MATERIALS CHEMISTRY FRONTIERS

CCS 中国化学会 CHINESE CHEMICAL SOCIETY

ICCAS

ROYAL SOCIETY OF CHEMISTRY

RESEARCH ARTICLE

View Article Online
View Journal | View Issue

Cite this: *Mater. Chem. Front.*, 2021, **5**, 3850

Hydrogen bond induced high-performance quaternary organic solar cells with efficiency up to 17.48% and superior thermal stability†

Xinrui Li,‡ Lei Zhou,‡ Xi Lu, Luye Cao, Xiaoyang Du,* Hui Lin, Caijun Zheng and Silu Tao*

Multicomponent systems have been widely investigated to expand absorption spectra, ameliorate morphology and achieve high-performance organic solar cells (OSCs). Here, we reveal a novel quaternary OSC based on a PM6:Y6:SR197:$PC_{71}BM$ system with a power conversion efficiency (PCE) of up to 17.48%, one of the highest efficiencies in organic photovoltaics. The N–H bonds of SR197 react with the F atom of acceptor Y6 to form intermolecular hydrogen bonds that regulate the morphology of the blended film and inhibit bimolecular recombination, so that a PCE of 16.83% is achieved for the ternary OSC based on a PM6:Y6:SR197 system. However, the PCE of PM6:Y6:$PC_{71}BM$-based devices is 16.72% due to the fullerene derivative $PC_{71}BM$ exhibiting strong isotropic transport ability. The quaternary OSC combines the advantages of the above two ternary devices, and it is noteworthy that SR197 can also form hydrogen bonds with $PC_{71}BM$, which allows targeted morphology control and improved device stability while increasing photon utilization. Therefore, the efficiency of the quaternary device rose by 12% in contrast to the binary device (15.56%). Our results detail the use of a hydrogen bonding strategy to overcome the disadvantages of the difficult-to-control morphology of multiple component devices, which is a valid way to achieve high-performance quaternary OSCs.

Received 3rd February 2021,
Accepted 12th March 2021

DOI: 10.1039/d1qm00197c

rsc.li/frontiers-materials

1. Introduction

Organic solar cells (OSCs) have been extensively researched on account of their transparency, low cost, and solution processability, as well as their potential for use in future sustainable development.[1–5] Through the design and synthesis of organic molecules, some successful non-fullerene materials have been synthesized, for instance ITIC, Y6, and their derivatives, which have contributed to the development of the organic photovoltaic field.[6–8] Nowadays, the efficiency of binary OSCs exceeds 17%.[9]

To further improve device efficiency, researchers have adopted different optimization methods, for example, the addition of solution additives,[10–13] the design of tandem devices,[14–17] and the use of multi-component strategies.[18–21] However, it is known that residual additives are extremely detrimental to OSC stability and the complex process of making tandem devices is not conducive to their future commercial production. In contrast, a multi-component strategy by introducing one or more guest materials into a bulk heterojunction layer, is an uncomplicated and valid method that can be used to boost device performance. An early ternary strategy was to adopt a third component as a guest to supplement the absorption of the host system, thereby increasing photon utilization and thus improving the current.[22–25] Based on this, quaternary devices and devices containing more components gradually emerged in order to continue enhancing the absorption in pursuit of high-efficiency OSCs.[26–33]

Currently, most of the quaternary OSCs in the reported articles are fabricated from two fullerene molecules and one non-fullerene molecule as the acceptor materials.[26,28,32,34] Among them, Liu *et al.* proposed a quaternary strategy of incorporating $PC_{61}BM$ as well as $PC_{71}BM$ into a PTB7-Th:IEICO-4F system. When fullerene materials are introduced as guest materials into a non-fullerene system this significantly improves the carrier mobility of the devices due to fullerene having good solubility and isotropic transport capability. The quaternary devices they prepared achieved a PCE of 12.52%, better than the control devices (9.67%).[28] However, fullerene itself has some disadvantages, such as poor stability and weak photon absorption capabilities. Therefore, the simultaneous selection of fullerene derivatives as the third and fourth components may not fully exploit the absorption spectrum

School of Optoelectronic Science and Engineering, University of Electronic Science and Technology of China (UESTC), Chengdu 610054, P. R. China.
E-mail: xiaoyangdu@uestc.edu.cn, silutao@uestc.edu.cn

† Electronic supplementary information (ESI) available. See DOI: 10.1039/d1qm00197c

‡ Xinrui Li and Lei Zhou contributed equally to this work.

because of their similar properties. Ma *et al.* chose non-fullerene Br-ITIC and the fullerene derivative $PC_{71}BM$ together as guest materials to dope into an active layer composed of PM6:Y6, and the PCE of the optimized quaternary devices was as high as 16.8%, one of the best efficiencies reported for organic photovoltaics.[29] Although this broadens the absorption spectrum, how to obtain an ideal active layer morphology is still a major challenge in multi-component devices.

In this study, we developed a successful design idea for quaternary devices by utilizing a hydrogen bonding strategy to directionally allocate the materials in the active layer and acquire excellent morphology. Through analysis, we found that the N–H groups of SR197 react with the F atoms of the acceptor Y6 to form hydrogen bonds, which selectively adjusts the film morphology and inhibits bimolecular recombination. Consequently, the PM6:Y6:SR197-based devices realized a PCE of 16.83%. In addition, due to the properties of the fullerene $PC_{71}BM$, the ternary OSCs based on the PM6:Y6:$PC_{71}BM$ system also exhibited a high PCE of 16.72%. On this basis, we chose SR197 and $PC_{71}BM$ as guest materials to incorporate into a PM6:Y6 system together. The introduction of the guest materials can directionally modify the morphology and improve the device stability while broadening the absorption spectrum, since hydrogen bonds can also be formed between SR197 and $PC_{71}BM$. can be formed which directional modify the film morphology and improve device stability while broadening the absorption spectrum. Ultimately, the quaternary OSCs achieved an efficiency of up to 17.48%, with a short-circuit current density (J_{SC}) of 27.11 mA cm^{-2}, an open-circuit voltage (V_{OC}) of 0.84 V, and a fill factor (FF) of 76.62%, which is much higher than that of the binary devices (15.56%). After heat treatment at 80 °C for 300 min, 85% of the original efficiency of the PM6:Y6:SR197:$PC_{71}BM$-based devices was retained, while the reference devices decayed to 69%. Our results show that combining a hydrogen bonding strategy with a quaternary strategy is a feasible method by which to achieve high-performance OSCs.

2. Results and discussion

2.1 Chemical and absorption properties of the materials

The molecular structures and energy levels of the components applied in the active layer are shown in Fig. 1 and 2a. The highest occupied molecular orbital (HOMO) levels of SR197 and $PC_{71}BM$ are −5.64 and −5.87 eV, respectively, while their lowest unoccupied molecular orbital (LUMO) levels are −3.62 and −3.91 eV, respectively. We note that the HOMOs and LUMOs of the two guest acceptors SR197 and $PC_{71}BM$ match with those of the main system, indicating that they are suitable to be added as the third and fourth components in a quaternary system. Moreover, the LUMO energy levels of both guest acceptors are higher than that of Y6, which is beneficial for improving the V_{OC} values of the devices.

Fig. 2b presents the absorption spectra of the active layer materials. Among them, the absorptions of SR197 and $PC_{71}BM$

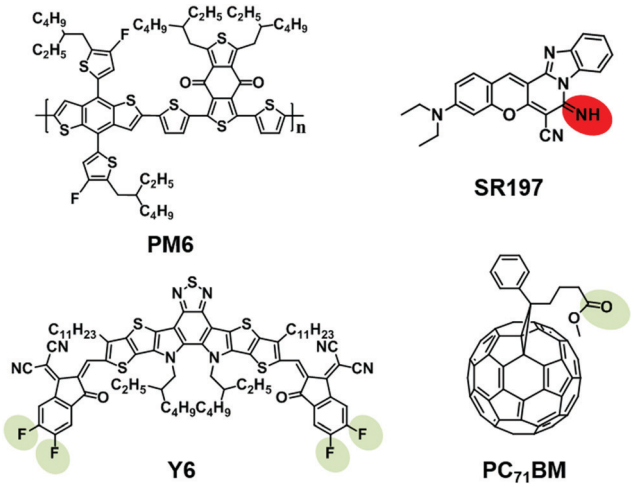

Fig. 1 Molecular structures of the active layer materials.

are mostly in the short wavelength range, at 430–650 nm and 350–700 nm, respectively. It can be seen that the absorption spectrum of the guest is supplementary with those of the hosts PM6 and Y6, contributing to the improved utilization of photons in the wider solar spectrum range of 300–1000 nm. The absorption spectra of the blended films are shown in Fig. 2c. We found that either the introduction of SR197 and $PC_{71}BM$ alone or together both enhanced the light absorption, especially in the 300–600 nm range, with the latter having a more pronounced effect on the absorption due to the absorption complementarity of the four components. It is worth noting that the introduction of the guest material slightly reduced the absorption of the blended film in the long wavelength range. This can be ascribed to the ratio of PM6 to Y6 of the host system changing from 1 : 1.2 to 1 : 1.1 when the third and fourth materials were doped.

The energy transfer of ternary and quaternary OSCs can be observed using the photoluminescence (PL) method. An important condition for Förster resonance energy transfer (FRET) energy transfer to occur is that the emission spectra of the guest material overlap with the absorption spectra of the other materials. Nonetheless, we do not provide PL for the pure Y6 film, the emission peak of which is mainly in the range of 900–1200 nm, as the test range of our instrument is 300–900 nm.[29,35] By comparing the absorption and PL spectra of the materials (Fig. 2b and Fig. S1a, ESI†), we found that the energy transfer may occur from $PC_{71}BM$ to Y6, SR197 to PM6 and SR197 to Y6. It has been reported that the incorporation of $PC_{71}BM$ in the PM6:Y6 system mainly affects the hole transfer from Y6 to PM6.[27] The energy transfer from SR197 to PM6 is also negligible, due to doped SR197 reducing the emission intensity of PM6 (Fig. S1b, ESI†). Furthermore, the PL spectra of pure SR197 as well as blended SR197:Y6 are shown in Fig. S1c (ESI†). Since the Y6 emission peak is not within our test conditions, a change in the Y6 emission peak was not observed. When excited at 560 nm, the emission peak of SR197 was located at around 700 nm. After excitation of the blended SR197:Y6 film using the same light, the emission peak of SR197 disappeared. Therefore, we have reason to believe that energy transfer between SR197 and Y6 occurred.

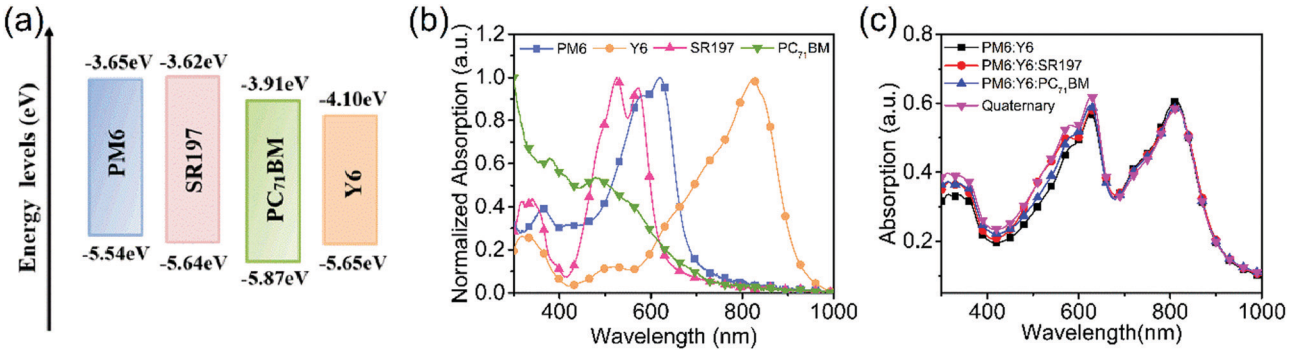

Fig. 2 (a) Energy level diagrams and (b) absorption spectra of the PM6, Y6, SR197, and $PC_{71}BM$ molecules. (c) The blended film absorption spectra for binary PM6:Y6, ternary PM6:Y6:SR197, ternary PM6:Y6:$PC_{71}BM$, and quaternary PM6:Y6:SR197:$PC_{71}BM$ system.

2.2 Photovoltaic properties

The current density–voltage (J–V) curves of the devices after doping SR197 as well as $PC_{71}BM$ into PM6:Y6 separately and together into the main system are shown in Fig. 3a, and the photovoltaic parameters of the homologous devices are listed in Table 1. For the ternary OSC-based PM6:Y6:SR197 system, after optimization, we obtained the best three-component ratio of 1 : 1.1 : 0.1 (Table S1, ESI†) and a corresponding maximum PCE of 16.83%. In addition, the optimal ratio of another ternary PM6:Y6:$PC_{71}BM$-based OSC was also 1 : 1.1 : 0.1 (Table S2, ESI†), exhibiting an optimal PCE of 16.72%. In order to further improving device performance, the two guest acceptors, SR197 and $PC_{71}BM$, were added into PM6:Y6 system together to prepare quaternary OSCs. The weight ratio of the four components in the active layer was optimized to 1 : 1.1 : 0.1 : 0.1 (Fig. S4 and Table S3, ESI†), and the quaternary OSCs combined the advantages of the ternary OSCs mentioned above. It can be visualized from Table 1 that the PCE of the quaternary OSCs was superior to those of the binary and ternary devices, respectively. Relative to the binary PM6:Y6-based devices (15.56%), the J_{SC} of the quaternary devices increased from 25.12 to 27.11 mA cm^{-2}, V_{OC} from 0.830 to 0.841 V, and FF from 74.53% to 76.62%, ultimately leading to a PCE of 17.48%, which is competitive to the values in the published literature.

Table 1 Photovoltaic performance parameters of OSCs based on binary PM6:Y6, ternary PM6:Y6:SR197, ternary PM6:Y6:$PC_{71}BM$ and quaternary PM6:Y6:SR197:$PC_{71}BM$ systems under simulated AM 1.5G (100 mW cm^{-2}) light illumination

Active layer	V_{OC} [V]	J_{SC} [mA cm^{-2}]	J_{cal} [mA cm^{-2}]	FF [%]	PCE [%]
PM6:Y6	0.830	25.12	24.89	74.53	15.56 (15.38)
PM6:Y6:SR197	0.834	26.87	25.88	75.08	16.83 (16.64)
PM6:Y6:$PC_{71}BM$	0.837	26.12	25.22	76.50	16.72 (16.61)
PM6:Y6:SR197:$PC_{71}BM$	0.841	27.11	26.02	76.62	17.48 (17.38)

The EQE characteristics of devices with/without the third and fourth components are visible in Fig. 3b. It can be found that adding SR197 and $PC_{71}BM$ separately and together to the main system both increased the EQE. And, among the four systems, the EQE curve of the quaternary OSCs was the highest. In the 420–500 nm wavelength range, the reinforcement was obvious. This apparent increase can be attributed to the incorporation of SR197, as it is just within the absorption spectrum of SR197. In addition to absorption complementarity, we speculate that the introduction of SR197 and of it together with $PC_{71}BM$ into the PM6:Y6 system leading to the improved device efficiency may be the cause of the intermolecular

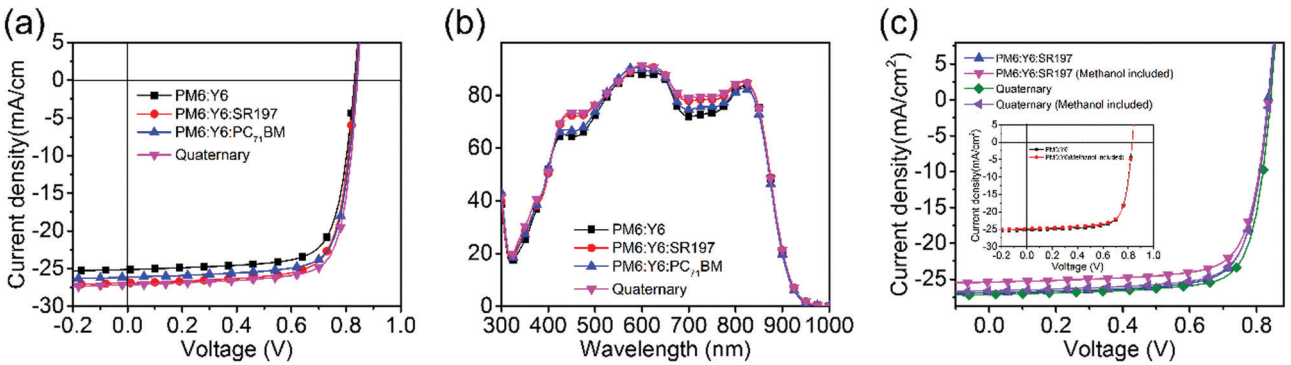

Fig. 3 (a) J–V and (b) EQE curves of the optimal OSCs based on binary PM6:Y6, ternary PM6:Y6:SR197, ternary PM6:Y6:$PC_{71}BM$ and quaternary PM6:Y6:SR197:$PC_{71}BM$ systems. (c) J–V curves of binary OSCs with and without hydrogen bonding inhibitor methanol (inset) and J–V curves of SR197-doped ternary as well as quaternary OSCs with and without hydrogen bonding inhibitor methanol.

interactions that the N–H group on SR197 can form with the O atom on $PC_{71}BM$ and the F atom on Y6, also known as hydrogen bonds. Therefore, the doping of guest materials as well as the existence of intermolecular hydrogen bonds raise the OSC charge transport and collection, optimizing the morphology of the blended film, thus enhancing the EQE in the range of 600–850 nm. The J_{SC} values calculated from the EQE spectra (J_{cal}) are within a reasonable error range from the actual measured J_{SC} values obtained.

2.3 Hydrogen bonds

To demonstrate that the improved performance indeed concerns the presence of hydrogen bonds, we added methanol to the active layer solution as a hydrogen bonding inhibitor to observe the change in device efficiency. As illustrated by Fig. 3c and Table S4 (ESI†), methanol had little effect on the control devices that do not contain hydrogen bonds. The PCEs of the binary OSCs were around 15.5% both before and after the addition of the inhibitor methanol. In contrast, when 0.5% methanol was doped into the PM6:Y6:SR197-based ternary OSCs, the performance changed significantly, from 16.83% to 15.84%. A similar downward trend was observed for the quaternary OSCs, where the device efficiency decreased from 17.48% to 16.69% after the addition of methanol. The above results illustrate that hydrogen bonds do exist between SR197 and the acceptors. Also, the presence of hydrogen bonds promotes the devices performance. It is believed that hydrogen bonding can improve the film morphology and increase the charge transport rate, which are mentioned in the later analysis.

2.4 Charge dynamics

So as to further study the influence of the multi-component strategy on the carrier dynamics, such as promoting exciton dissociation and charge extraction, we measured the photocurrent density (J_{ph}) and effective voltage (V_{eff}), and the curves are shown in Fig. 4a. J_{ph} is defined by the formula $J_L - J_D$, in which J_L is the photocurrent density in a light environment, and J_D is that in the dark. V_{eff} is calculated from $V_0 - V_{bias}$, in which the voltage value V_0 is obtained when the J_{ph} value is equal to zero, and the voltage bias applied from the outside is regarded as V_{bias}. When the V_{eff} is large enough, the electrode can fully extract photogenerated carriers and the J_{ph} approaches the saturation value (J_{sat}). The J_{SC}/J_{sat} value under short-circuit conditions represents the probability of charge dissociation (η_{diss}).[36,37] After calculation, the η_{diss} values of the binary, SR197-based ternary, $PC_{71}BM$-based ternary and quaternary OSCs were obtained as 0.964, 0.973, 0.975 and 0.980, respectively. In addition, the J_{power}/J_{sat} value can be used to understand the charge collection efficiency (η_{coll}), in which J_{power} is the current density value when the applied voltage is multiplied by its corresponding current to take the maximum. The η_{coll} values obtained for the binary, SR197-based ternary, $PC_{71}BM$-based ternary and quaternary OSCs were 0.860, 0.861, 0.872 and 0.873, respectively. It can be seen that the quaternary OSCs prepared by the simultaneous introduction of SR197 as well as $PC_{71}BM$ further improve the exciton dissociation and charge collection compared to the binary and ternary devices, which is closely related to the formation of intermolecular interactions.

A space-charge-limited current (SCLC) investigation was carried out to further research the effect that the intermolecular hydrogen bonds formed by adding SR197 and $PC_{71}BM$ into the host system have on the charge transfer properties (Table S5, ESI† and Fig. 4b and c).[38] After adding SR197 or $PC_{71}BM$ into the PM6:Y6 system, the hole mobility of the obtained blended membranes was slightly improved, increasing from 2.90×10^{-4} cm^2 V^{-1} s^{-1} to 3.65×10^{-4} cm^2 V^{-1} s^{-1} and to 3.49×10^{-4} cm^2 V^{-1} s^{-1}, respectively. However, compared with the control device, the electron mobility of the PM6:Y6:SR197 film also rose from 6.67×10^{-5} to 1.02×10^{-4} cm^2 V^{-1} s^{-1}, while that of PM6:Y6:$PC_{71}BM$ film increased to 9.07×10^{-5} cm^2 V^{-1} s^{-1}. Moreover, introducing both SR197 and $PC_{71}BM$, the hole and electron mobility were further enhanced, which were measured to be 4.01×10^{-4} and 1.18×10^{-4} cm^2 V^{-1} s^{-1}, respectively. And, the corresponding μ_h and μ_e ratio was more balanced. These consequences show that the addition of double guest acceptors can effectively raise the mobility of the reference system, achieving greater matched charge transport, thus enhancing the J_{SC} and FF values.

2.5 Film morphology

In order to better determine the reasons for the change in device performance, we employed AFM and TEM to observe the

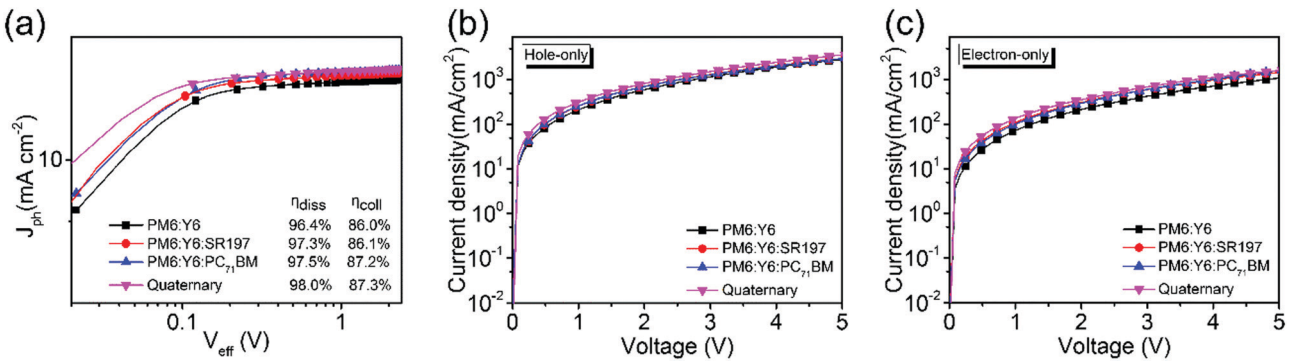

Fig. 4 (a) J_{ph} *versus* V_{eff} curves of OSCs based on the binary PM6:Y6, ternary PM6:Y6:SR197, ternary PM6:Y6:$PC_{71}BM$ and quaternary PM6:Y6:SR197:$PC_{71}BM$ systems. (b) Hole and (c) electron mobilities of the binary, ternary and quaternary blended films.

morphology of the active layer, as indicated in Fig. 5. Phase and height images recorded using AFM are used to observe film surface morphology and roughness. As shown in Fig. 5a and b, the relatively large phase separation of the pure binary film can be observed, with a corresponding roughness of 3.54 nm. When SR197 was doped into the host PM6:Y6 system, the phenomenon of excessive phase separation was somewhat alleviated and the roughness of the ternary film was 2.18 nm. In addition, the phase of the ternary film based on PM6:Y6:$PC_{71}BM$ was similar to that of PM6:Y6:SR197. In comparison with the control device, the film morphology was improved to some extent, with a roughness of 2.26 nm. It is clear from the previous photovoltaic parameters that both OSCs based on these two ternary systems showed increased current values compared to the binary devices. These results reveal that the charge transport is mainly reliant on the Y6 transport channel, but that the doping of either SR197 or $PC_{71}BM$ provides an auxiliary channel to help the charge transmission. When SR197 and $PC_{71}BM$ were mixed into PM6:Y6 system together, the quaternary co-blended film had the best morphology, with the smoothest surface relative to a roughness of 1.55 nm, which is conducive to exciton dissociation and charge transport. The above changes for the four film morphology based on different systems conform to the device performance trend, therefore showing that the quaternary OSCs with the optimal morphology exhibited the highest current value and fill factor.

The TEM characteristics of the blended films based on various systems are presented in Fig. 5c. For the binary blended films based on PM6:Y6, some obvious aggregation phenomena can be observed. However, when SR197 or $PC_{71}BM$ was doped, it was found that the aggregation phenomenon was improved and that a nanofiber structure was formed in the films. For the PM6:Y6:SR197 ternary blend film, this may be due to the intermolecular interaction between the N–H group on SR197 and the F atom on Y6, which promotes an improvement in the morphology. When it comes to the PM6:Y6:$PC_{71}BM$ ternary blended film, the optimization of the morphology is mainly due to the existence of fullerene $PC_{71}BM$, which is isotropic and has excellent electron acceptance and electron transmission characteristics. Furthermore, when SR197 and $PC_{71}BM$ were incorporated together, a more uniform nanofiber network structure as well as proper phase separation can be observed. This is owing to the fact that the N–H group on SR197 can form intermolecular interactions with both Y6 and $PC_{71}BM$, which not only promotes better miscibility of the acceptors in the quaternary blended films, but also modulates the film morphology, forming continuous charge transport channels, and ultimately increasing the transport capacity of the holes and electrons.

To further examine the effect of molecular interaction on the morphology of the films, grazing-incidence wide-angle X-ray scattering (GIWAXS) measurements were carried out to observe molecular crystallization and stacking. Fig. 6a–d illustrate the 2D GIWAXS images for the PM6:Y6-based, PM6:Y6:SR197-based, PM6:Y6:$PC_{71}BM$-based, and PM6:Y6:SR197:PC_{71}BM-based films, respectively. Fig. 6e and f are the out-of-plane (OOP) and in-plane (IP) direction linear cut sections of the blended films, respectively. In films based on different

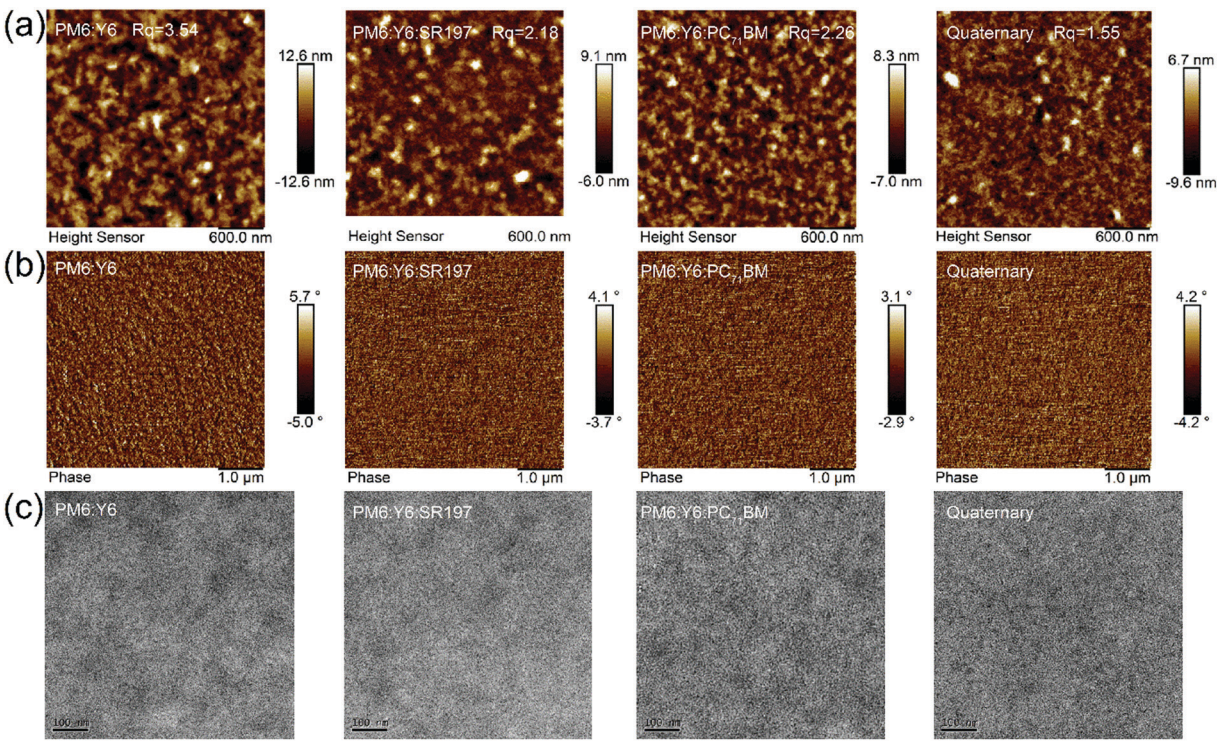

Fig. 5 (a) AFM height images, (b) AFM phase images and (c) TEM images of the blended films based on the binary PM6:Y6, ternary PM6:Y6:SR197, ternary PM6:Y6:$PC_{71}BM$ and quaternary PM6:Y6:SR197:$PC_{71}BM$ systems, respectively.

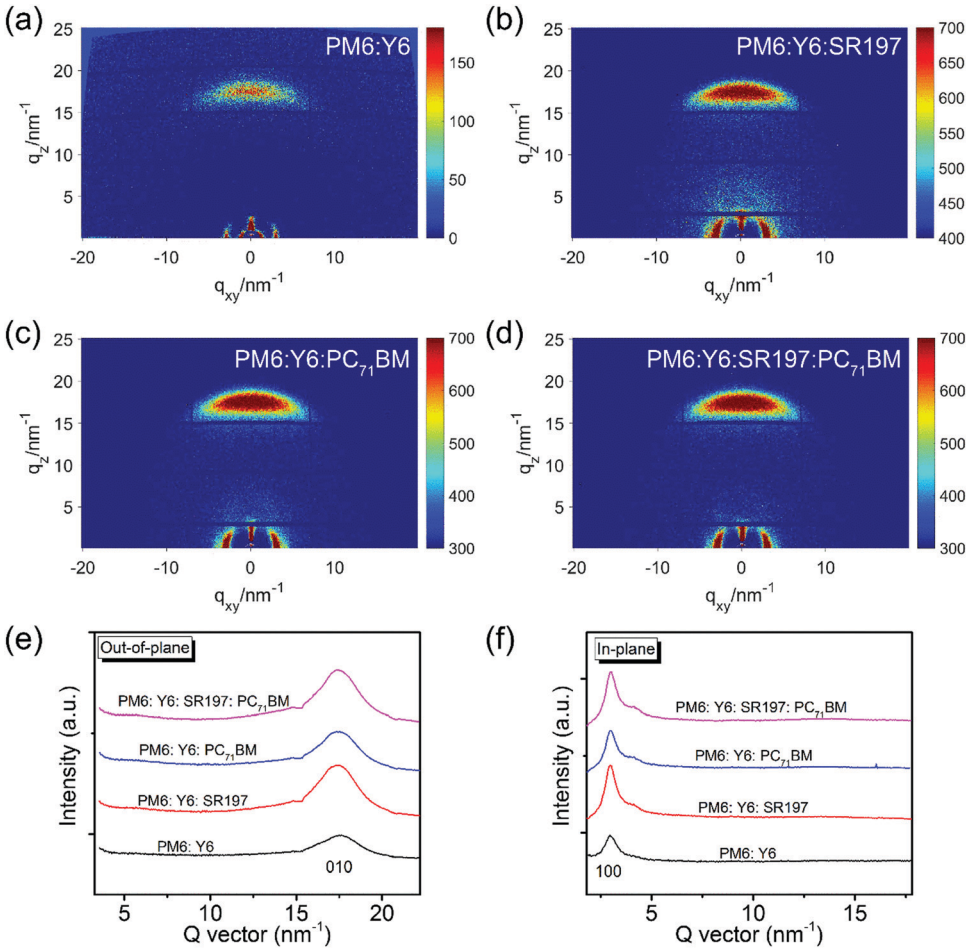

Fig. 6 (a–d) 2D GIWAXS of the blended films of the binary PM6:Y6, ternary PM6:Y6:SR197, ternary PM6:Y6:$PC_{71}BM$ and quaternary PM6:Y6:SR197:$PC_{71}BM$ systems. (e) 1D GIWAXS out-of-plane and (f) in-plane data of the different blended films.

systems, we both observed the OOP (010) diffraction summit at 17.57 nm^{-1} and IP (100) diffraction summit at 3.1 nm^{-1}, which is consistent with the diffraction peak of the pure PM6 film,[29,39] indicating that the doping of small molecular acceptors does not disturb the arrangement and crystallization of the PM6 molecules. The intensity of the OOP (010) diffraction peaks as well as the IP (100) diffraction peaks are relatively stronger for the ternary and quaternary films compared to the binary films, and that of the quaternary film is particularly obvious. Using the Scherrer equation,[40,41] the π–π stacking crystal correlation length (CCL) in the OOP direction for the blended films based using the binary, SR197-based ternary, $PC_{71}BM$-based ternary, quaternary systems were calculated to be 1.08, 1.56, 1.22 and 1.69 nm, respectively. It is evident that the introduction of the guest acceptors, especially SR197, which can form intermolecular hydrogen bonds with the host system, enhances the crystal domain size and makes the molecular arrangement more orderly to provide a neat path for charge transport, which is why the FF values of the quaternary OSCs increased.

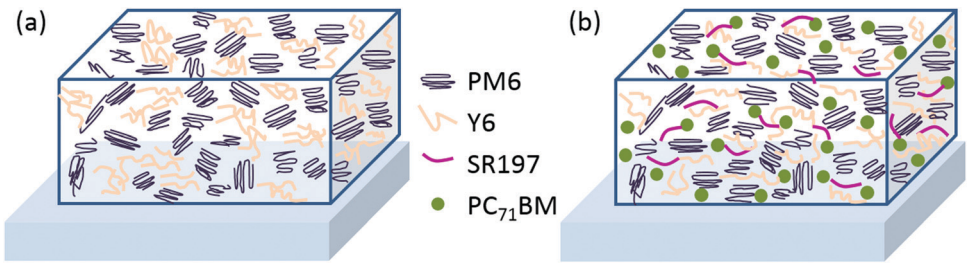

Fig. 7 Schematic diagrams of the morphological characteristics of the blended films for (a) the binary PM6:Y6-based OSCs and (b) the quaternary PM6:Y6:SR197:$PC_{71}BM$-based OSCs.

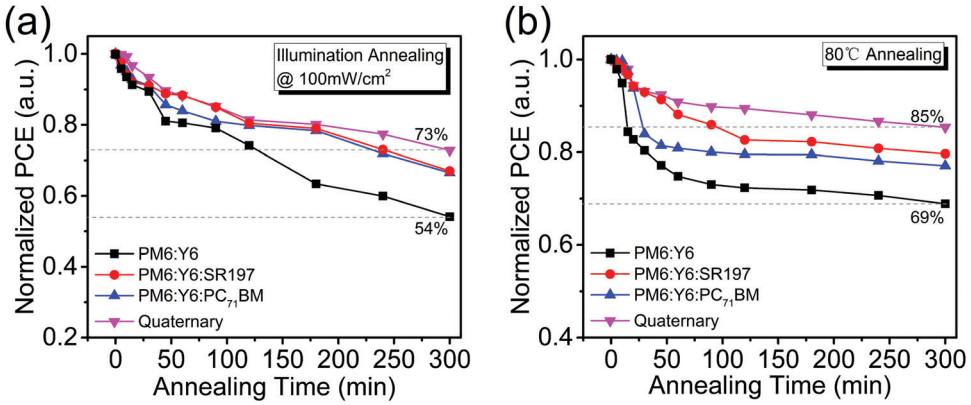

Fig. 8 (a) Light stability and (b) thermal stability of devices based on different systems.

Based on the conclusions obtained from the above-mentioned morphology tests, we can simulate the material distribution in the active layer of the binary and quaternary devices, as illustrated in Fig. 7a and b. Since the end group of the Y6 molecule contains F atoms with strong electron-absorbing ability, the molecules are prone to aggregation. Therefore, in the binary blended films based on the PM6:Y6 system, defects and traps unfavorable to exciton dissociation and charge transport are formed. When SR197 and $PC_{71}BM$ were introduced, the morphology of the quaternary films was significantly improved. Firstly, the solubility of the two guest materials is outstanding, and due to the presence of hydrogen bonding, SR197 "hold hands" with $PC_{71}BM$ and Y6, driving the Y6 molecules to be uniformly distributed in the active layer, increasing the contact surface between the donor and the acceptor, furthermore accelerating exciton dissociation. At the same time, the doping of the guests does not destroy the donor crystallization, so it has no adverse effect on the charge transport, which is consistent with the previous charge dynamics analysis.

2.6 Stability

In order to understand the influence that intermolecular interactions formed after the doping of SR197 and $PC_{71}BM$ have on device stability, we evaluated the light and thermal stability of the unencapsulated devices in an atmospheric environment. Light stability was gauged under one sunlight illumination and the thermal stability was gauged under 80 °C substrate heating. As listed in Fig. 8a, after 300 min of continuous irradiation, OSCs based on different systems showed varying degrees of degradation. Among them, the degradation rate of the PM6:Y6-based devices is the fastest, with an efficiency of only 54% of the initial efficiency after 300 mins. The unfavorable stability limits the practical application of the devices. In addition to this, the efficiency of both the PM6:Y6:SR197-based and the PM6:Y6:$PC_{71}BM$-based OSCs decayed to around 65% of the initial efficiency. By contrast, the photostability of the quaternary OSCs was best. After 300 minutes of light exposure, the efficiency of the device was still 73% of its initial value.

A graph of the thermal stability change is given in Fig. 8b. For the control OSCs and PM6:Y6:$PC_{71}BM$-based OSCs, the device efficiency decayed rapidly in the first 30 minutes. After 300 minutes of heat treating at 80 °C, the PCEs of the control devices had decayed to 69% of their original efficiency, while the ternary and quaternary OSCs containing SR197 exhibited better thermal stability. Notably, the quaternary OSCs retained 85% of their initial performance after heating at 80 °C for 300 min. The above results show that intermolecular interactions can improve photostability and thermal stability to some extent, especially thermal stability. This may be due to the presence of hydrogen bonds, which optimizes the distribution of molecules in the active layer, resulting in the film morphology remaining unchanged when the external environment is changed, thus optimizing the stability.[42]

3. Conclusions

We prepared a novel quaternary OSC *via* adding SR197 and $PC_{71}BM$ into the host system (PM6:Y6) and achieved a PCE of up to 17.48%, one of the highest efficiencies in the organic photovoltaics field. The quaternary system combines the advantages of the two ternary PM6:Y6:SR197 and PM6:Y6:$PC_{71}BM$ systems. Among them, the N–H group of SR197 and the F atom of Y6 form intermolecular hydrogen bonds (N–H···F), which modulate the blended film morphology and inhibit bimolecular recombination, resulting in a PCE of 16.83% for ternary PM6:Y6:SR197-based OSCs. Moreover, the PCE of the ternary OSC based on the PM6:Y6:$PC_{71}BM$ system is 16.72% due to the fullerene derivative $PC_{71}BM$ having good solubility and strong isotropic transport capacity, as well as other advantages. Therefore, the efficiency of the quaternary devices prepared by doping $PC_{71}BM$ together with SR197 into PM6:Y6 is much better than that of binary devices (15.56%) with the J_{SC} value increasing from 25.12 to 27.11 mA cm^{-2} and the FF value from 74.53% to 76.62%. It is noteworthy that $PC_{71}BM$ can also form hydrogen bonds with SR197, which directionally regulates the active layer morphology and the interaction of the guest materials with the host system enhances donor crystallization, facilitates charge transport and collection. Consequently, our work details an effective method by which to select suitable quaternary components to prepare high-performance OSCs.

4. Experimental section

Details about the materials, device preparation, and experimental methods covered in this paper are in the ESI.†

Conflicts of interest

The authors declare no conflict of interest.

Acknowledgements

The work was supported by the National Natural Science Foundation of China (NSFC Grant No. 62075029, 61775029, and 51533005), the International Cooperation and Exchange Project of Science and Technology Department of Sichuan Province (2019YFH0059), the Shanghai Natural Science Foundation and Sailing Program (No. 19ZR1463300 and 17YF1400600), and the China Postdoctoral Science Foundation (2020TQ0058).

Notes and references

1 H. Jinno, K. Fukuda, X. Xu, S. Park, Y. Suzuki, M. Koizumi, T. Yokota, I. Osaka, K. Takimiya and T. Someya, Stretchable and waterproof elastomer-coated organic photovoltaics for washable electronic textile applications, *Nat. Energy*, 2017, **2**, 780–785.

2 Q. Xue, R. Xia, C. J. Brabec and H.-L. Yip, Recent advances in semi-transparent polymer and perovskite solar cells for power generating window applications, *Energy Environ. Sci.*, 2018, **11**, 1688–1709.

3 A. Polman, M. Knight, E. C. Garnett, B. Ehrler and W. C. Sinke, Photovoltaic materials: present efficiencies and future challenges, *Science*, 2016, **352**, aad4424.

4 Z. Hu, J. Wang, X. Ma, J. Gao, C. Xu, K. Yang, Z. Wang, J. Zhang and F. Zhang, A critical review on semitransparent organic solar cells, *Nano Energy*, 2020, **78**, 105376.

5 Q. Fan, Q. An, Y. Lin, Y. Xia, Q. Li, M. Zhang, W. Su, W. Peng, C. Zhang, F. Liu, L. Hou, W. Zhu, D. Yu, M. Xiao, E. Moons, F. Zhang, T. D. Anthopoulos, O. Inganäs and E. Wang, Over 14% efficiency all-polymer solar cells enabled by a low bandgap polymer acceptor with low energy loss and efficient charge separation, *Energy Environ. Sci.*, 2020, **13**, 5017–5027.

6 Y. Lin, J. Wang, Z. G. Zhang, H. Bai, Y. Li, D. Zhu and X. Zhan, An electron acceptor challenging fullerenes for efficient polymer solar cells, *Adv. Mater.*, 2015, **27**, 1170–1174.

7 X. Xu, K. Feng, Z. Bi, W. Ma, G. Zhang and Q. Peng, Single-Junction Polymer Solar Cells with 16.35% Efficiency Enabled by a Platinum(II) Complexation Strategy, *Adv. Mater.*, 2019, **31**, 1901872.

8 L. Nian, Y. Kan, H. Wang, K. Gao, B. Xu, Q. Rong, R. Wang, J. Wang, F. Liu, J. Chen, G. Zhou, T. P. Russell and A. K. Y. Jen, Ternary non-fullerene polymer solar cells with 13.51% efficiency and a record-high fill factor of 78.13%, *Energy Environ. Sci.*, 2018, **11**, 3392–3399.

9 Q. Liu, Y. Jiang, K. Jin, J. Qin, J. Xu, W. Li, J. Xiong, J. Liu, Z. Xiao, K. Sun, S. Yang, X. Zhang and L. Ding, 18% Efficiency organic solar cells, *Sci. Bull.*, 2020, **65**, 272–275.

10 X. Song, N. Gasparini, L. Ye, H. Yao, J. Hou, H. Ade and D. Baran, Controlling Blend Morphology for Ultrahigh Current Density in Nonfullerene Acceptor-Based Organic Solar Cells, *ACS Energy Lett.*, 2018, **3**, 669–676.

11 C.-M. Liu, Y.-W. Su, J.-M. Jiang, H.-C. Chen, S.-W. Lin, C.-J. Su, U. S. Jeng and K.-H. Wei, Complementary solvent additives tune the orientation of polymer lamellae, reduce the sizes of aggregated fullerene domains, and enhance the performance of bulk heterojunction solar cells, *J. Mater. Chem. A*, 2014, **2**, 20760–20769.

12 X. Xu, T. Yu, Z. Bi, W. Ma, Y. Li and Q. Peng, Realizing Over 13% Efficiency in Green-Solvent-Processed Nonfullerene Organic Solar Cells Enabled by 1,3,4-Thiadiazole-Based Wide-Bandgap Copolymers, *Adv. Mater.*, 2018, **30**, 1703973.

13 C. Liao, M. Zhang, X. Xu, F. Liu, Y. Li and Q. Peng, Green solvent-processed efficient non-fullerene organic solar cells enabled by low-bandgap copolymer donors with EDOT side chains, *J. Mater. Chem. A*, 2019, **7**, 716–726.

14 L. Meng, Y. Zhang, X. Wan, C. Li, X. Zhang, Y. Wang, X. Ke, Z. Xiao, L. Ding, R. Xia, H.-L. Yip, Y. Cao and Y. Chen, Organic and solution-processed tandem solar cells with 17.3% efficiency, *Science*, 2018, **361**, 1094.

15 Y. Cui, H. Yao, B. Gao, Y. Qin, S. Zhang, B. Yang, C. He, B. Xu and J. Hou, Fine-Tuned Photoactive and Interconnection Layers for Achieving over 13% Efficiency in a Fullerene-Free Tandem Organic Solar Cell, *J. Am. Chem. Soc.*, 2017, **139**, 7302–7309.

16 M. B. Salim, R. Nekovei and R. Jeyakumar, Organic tandem solar cells with 18.6% efficiency, *Sol. Energy*, 2020, **198**, 160–166.

17 M. M. Li, K. Gao, X. J. Wan, Q. Zhang, B. Kan, R. X. Xia, F. Liu, X. Yang, H. R. Feng, W. Ni, Y. C. Wang, J. J. Peng, H. T. Zhang, Z. Q. Liang, H. L. Yip, X. B. Peng, Y. Cao and Y. S. Chen, Solution-processed organic tandem solar cells with power conversion efficiencies >12%, *Nat. Photonics*, 2017, **11**, 85–90.

18 X. Wang, Q. Sun, J. Gao, X. Ma, J. H. Son, S. Y. Jeong, Z. Hu, L. Niu, H. Y. Woo, J. Zhang and F. Zhang, Ternary Organic Photovoltaic Cells Exhibiting 17.59% Efficiency with Two Compatible Y6 Derivations as Acceptor, *Sol. RRL*, 2021, **05**, 2100007.

19 M. Xiao, K. Zhang, S. Dong, Q. Yin, Z. Liu, L. Liu, F. Huang and Y. Cao, High-Performance Ternary Nonfullerene Polymer Solar Cells with Both Improved Photon Harvesting and Device Stability, *ACS Appl. Mater. Interfaces*, 2018, **10**, 25594–25603.

20 X. Du, Y. Yuan, L. Zhou, H. Lin, C. Zheng, J. Luo, Z. Chen, S. Tao and L. S. Liao, Delayed Fluorescence Emitter Enables Near 17% Efficiency Ternary Organic Solar Cells with Enhanced Storage Stability and Reduced Recombination Energy Loss, *Adv. Funct. Mater.*, 2020, **30**, 1909837.

21 M. Zhang, L. Zhu, G. Zhou, T. Hao, C. Qiu, Z. Zhao, Q. Hu, B. W. Larson, H. Zhu, Z. Ma, Z. Tang, W. Feng, Y. Zhang, T. P. Russell and F. Liu, Single-layered organic photovoltaics with double cascading charge transport pathways: 18% efficiencies, *Nat. Commun.*, 2021, **12**, 309.

22 K. Li, Y. Wu, Y. Tang, M. A. Pan, W. Ma, H. Fu, C. Zhan and J. Yao, Ternary Blended Fullerene-Free Polymer Solar Cells with 16.5% Efficiency Enabled with a Higher-LUMO-Level Acceptor to Improve Film Morphology, *Adv. Energy Mater.*, 2019, **9**, 1901728.

23 Y. Ma, X. Zhou, D. Cai, Q. Tu, W. Ma and Q. Zheng, A minimal benzo[*c*][1,2,5]thiadiazole-based electron acceptor as a third component material for ternary polymer solar cells with efficiencies exceeding 16.0%, *Mater. Horiz.*, 2020, **7**, 117–124.

24 Z.-X. Liu, T.-K. Lau, G. Zhou, S. Li, J. Ren, S. K. Das, R. Xia, G. Wu, H. Zhu, X. Lu, H.-L. Yip, H. Chen and C.-Z. Li, Achieving efficient organic solar cells and broadband photodetectors via simple compositional tuning of ternary blends, *Nano Energy*, 2019, **63**, 103807.

25 H. Jiang, X. Li, H. Wang, Z. Ren, N. Zheng, X. Wang, Y. Li, W. Chen and R. Yang, Significantly Enhanced Molecular Stacking in Ternary Bulk Heterojunctions Enabled by an Appropriate Side Group on Donor Polymer, *Adv. Sci.*, 2020, **7**, 1903455.

26 D. Yan, J. Xin, W. Li, S. Liu, H. Wu, W. Ma, J. Yao and C. Zhan, 13%-Efficiency Quaternary Polymer Solar Cell with Nonfullerene and Fullerene as Mixed Electron Acceptor Materials, *ACS Appl. Mater. Interfaces*, 2019, **11**, 766–773.

27 K. Li, Y. Wu, X. Li, H. Fu and C. Zhan, 17.1%-Efficiency organic photovoltaic cell enabled with two higher-LUMO-level acceptor guests as the quaternary strategy, *Sci. China: Chem.*, 2020, **63**, 490–496.

28 L. Liu, H. Chen, W. Chen and F. He, From binary to quaternary: high-tolerance of multi-acceptors enables development of efficient polymer solar cells, *J. Mater. Chem. A*, 2019, **7**, 7815–7822.

29 X. Ma, J. Wang, Q. An, J. Gao, Z. Hu, C. Xu, X. Zhang, Z. Liu and F. Zhang, Highly efficient quaternary organic photovoltaics by optimizing photogenerated exciton distribution and active layer morphology, *Nano Energy*, 2020, **70**, 104496.

30 L. Arunagiri, Z. Peng, X. Zou, H. Yu, G. Zhang, Z. Wang, J. Y. Lin Lai, J. Zhang, Y. Zheng, C. Cui, F. Huang, Y. Zou, K. S. Wong, P. C. Y. Chow, H. Ade and H. Yan, Selective Hole and Electron Transport in Efficient Quaternary Blend Organic Solar Cells, *Joule*, 2020, **4**, 1790–1805.

31 S.-C. Shin, P. Vincent, J.-H. Bae, J. J. Lee, M. Nam, D.-H. Ko, H. Kim and J. W. Shim, Quaternary indoor organic photovoltaic device demonstrating panchromatic absorption and power conversion efficiency of 10%, *Dyes Pigm.*, 2019, **163**, 48–54.

32 W. Li, D. Yan, F. Liu, T. Russell, C. Zhan and J. Yao, High-efficiency quaternary polymer solar cells enabled with binary fullerene additives to reduce nonfullerene acceptor optical band gap and improve carriers transport, *Sci. China: Chem.*, 2018, **61**, 1609–1618.

33 X. Xu, Z. Li, Z. Wang, K. Li, K. Feng and Q. Peng, 10.20% Efficiency polymer solar cells *via* employing bilaterally hole-cascade diazaphenanthrobisthiadiazole polymer donors and electron-cascade indene-C70 bisadduct acceptor, *Nano Energy*, 2016, **25**, 170–183.

34 F. Shen, D. Yan, W. Li, H. Meng, J. Huang, X. Li, J. Xu and C. Zhan, Quaternary polymer solar cells with over 13% efficiency enabled by improving film-morphologiesviabinary mixed fullerene additive, *Mater. Chem. Front.*, 2019, **3**, 301–307.

35 Z.-C. Wen, H. Yin and X.-T. Hao, Recent progress of PM6:Y6-based high efficiency organic solar cells, *Surf. Interfaces*, 2021, **23**, 100921.

36 P. W. M. Blom, V. D. Mihailetchi, L. J. A. Koster and D. E. Markov, Device physics of polymer: fullerene bulk heterojunction solar cells, *Adv. Mater.*, 2007, **19**, 1551–1566.

37 H. Yu, R. Ma, Y. Xiao, J. Zhang, T. Liu, Z. Luo, Y. Chen, F. Bai, X. Lu, H. Yan and H. Lin, Improved organic solar cell efficiency based on the regulation of an alkyl chain on chlorinated non-fullerene acceptors, *Mater. Chem. Front.*, 2020, **4**, 2428–2434.

38 C. Melzer, E. J. Koop, V. D. Mihailetchi and P. W. M. Blom, Hole Transport in Poly(phenylene vinylene)/Methanofullerene Bulk-Heterojunction Solar Cells, *Adv. Funct. Mater.*, 2004, **14**, 865–870.

39 J. Yuan, Y. Zhang, L. Zhou, G. Zhang, H.-L. Yip, T.-K. Lau, X. Lu, C. Zhu, H. Peng, P. A. Johnson, M. Leclerc, Y. Cao, J. Ulanski, Y. Li and Y. Zou, Single-Junction Organic Solar Cell with over 15% Efficiency Using Fused-Ring Acceptor with Electron-Deficient Core, *Joule*, 2019, **3**, 1140–1151.

40 J. T. Rogers, K. Schmidt, M. F. Toney, E. J. Kramer and G. C. Bazan, Structural order in bulk heterojunction films prepared with solvent additives, *Adv. Mater.*, 2011, **23**, 2284–2288.

41 K. Kawashima, T. Fukuhara, Y. Suda, Y. Suzuki, T. Koganezawa, H. Yoshida, H. Ohkita, I. Osaka and K. Takimiya, Implication of Fluorine Atom on Electronic Properties, Ordering Structures, and Photovoltaic Performance in Naphthobisthiadiazole-Based Semiconducting Polymers, *J. Am. Chem. Soc.*, 2016, **138**, 10265–10275.

42 X. Xu, J. Xiao, G. Zhang, L. Wei, X. Jiao, H.-L. Yip and Y. Cao, Interface-enhanced organic solar cells with extrapolated T80 lifetimes of over 20 years, *Sci. Bull.*, 2020, **65**, 208–216.

